

# Real-time quantitative imaging of failure events in materials under load at temperatures above 1,600 °C

Hrishikesh A. Bale<sup>1</sup>, Abdel Haboub<sup>2</sup>, Alastair A. MacDowell<sup>2</sup>, James R. Nasiatka<sup>2</sup>, Dilworth Y. Parkinson<sup>2</sup>, Brian N. Cox<sup>3</sup>, David B. Marshall<sup>3</sup> and Robert O. Ritchie<sup>1,2\*</sup>

**Ceramic matrix composites are the emerging material of choice for structures that will see temperatures above ~1,500 °C in hostile environments, as for example in next-generation gas turbines and hypersonic-flight applications. The safe operation of applications depends on how small cracks forming inside the material are restrained by its microstructure. As with natural tissue such as bone and seashells, the tailored microstructural complexity of ceramic matrix composites imparts them with mechanical toughness, which is essential to avoiding failure. Yet gathering three-dimensional observations of damage evolution in extreme environments has been a challenge. Using synchrotron X-ray computed microtomography, we have fully resolved sequences of microcrack damage as cracks grow under load at temperatures up to 1,750 °C. Our observations are key ingredients for the high-fidelity simulations used to compute failure risks under extreme operating conditions.**

X-ray computed microtomography ( $\mu$ -CT), using the high fluxes from synchrotron sources, has evolved into a powerful imaging tool in the fields of physical and biological sciences from its ability to image structure in three dimensions with high spatial resolution at macroscopic to submicroscopic scales<sup>1,2</sup>. With the development of increasingly complex structural materials, such as fibre-reinforced ceramic composites and polymer-matrix composites, that are finding increasing use in cutting-edge aerospace applications<sup>3–7</sup>, three-dimensional (3D) characterization of both structure and damage processes is essential, for it is the geometry, scale and nature of these structures in all three dimensions that control their properties.

The past decade has witnessed the emergence of strong and tough ceramic matrix composites, within which various design strategies are used on different spatial scales to overcome the brittleness that is inherent in materials that are able to survive extreme temperatures and chemically corrosive environments. Strong continuous fibre bundles (scale 0.1–1 mm) are woven in custom-designed 3D patterns, with individual bundles oriented in space so that they will follow the primary load paths expected in a given component to maximize its strength, and interlocked with one another to prevent catastrophic separation when damaged<sup>3</sup>. Larger interstices between the fibre bundles may be partially filled with randomly oriented fine reinforcing rods (scale, 1–10  $\mu$ m), inhibiting local cracking under thermal shock. Coatings applied to individual fibres (scale, 0.1–1  $\mu$ m) inhibit chemical reactions and ensure that the interfaces between the fibres and the matrix remain weak, allowing a ductile response through matrix cracking and frictional pullout of crack-bridging fibres. The remaining space between coated fibres, fibre bundles, and reinforcing rods is filled with a ceramic matrix material, which itself may be a hybrid containing, for example, graphitic sheets that inhibit oxygen ingress (scale, 1–100 nm; ref. 8). Thus, like many natural materials, these

new ceramic composites achieve robustness through complexity: their hierarchical, hybrid microstructure impedes the growth of local damage and prevents the large fatal cracks that are characteristic of brittle materials.

However, complexity in composition brings complexity in safe use. Most engineering structures, airframes, ships, buildings and so on, are designed to tolerate quite large cracks, which can be safely left monitored but unattended if they are less than a critical length; for example, 10 mm or more in an airframe. Such cracks are large compared with the internal microstructural heterogeneity of a conventional material, which makes the prediction of their growth relatively easy; the effects of heterogeneity on crack growth tend to average out and therefore need not be included explicitly in engineering safety codes<sup>9</sup>. For ceramic composites in ultrahigh-temperature applications, especially where corrosive species in the environment must be kept out of the material, relatively small cracks, on the order of the thickness of a fibre bundle (~1 mm), can be unacceptable. These new ceramic materials thus violate the simplifying maxim of most traditional materials, that they be considered homogeneous on the scale at which damage becomes critical.

Exactly how microcracks are restrained by such a tailored microstructure becomes the central question for the materials scientist, who seeks to find the optimal composition or architecture, and the design engineer, who must predict the failure envelope. These questions raise many challenges: the conditions of interest are extreme. Observational methods based on direct imaging of the surface are complicated by high thermal noise (however, see a recent breakthrough in optical digital-image correlation performed at 1,500 °C; ref. 10). The properties (strength, and so on) of the composite's constituent materials and their interfaces are generally unknown at high temperature; they are also impossible to calibrate by independent tests, because the strength of different phases combined at nanometre and micrometre scales is not

<sup>1</sup>Department of Materials Science and Engineering, University of California, Berkeley, California 94720, USA, <sup>2</sup>Lawrence Berkeley National Laboratory, Berkeley, California 94720, USA, <sup>3</sup>Teledyne Scientific Company, Thousand Oaks, California 91360, USA. \*e-mail: roritche@lbl.gov.

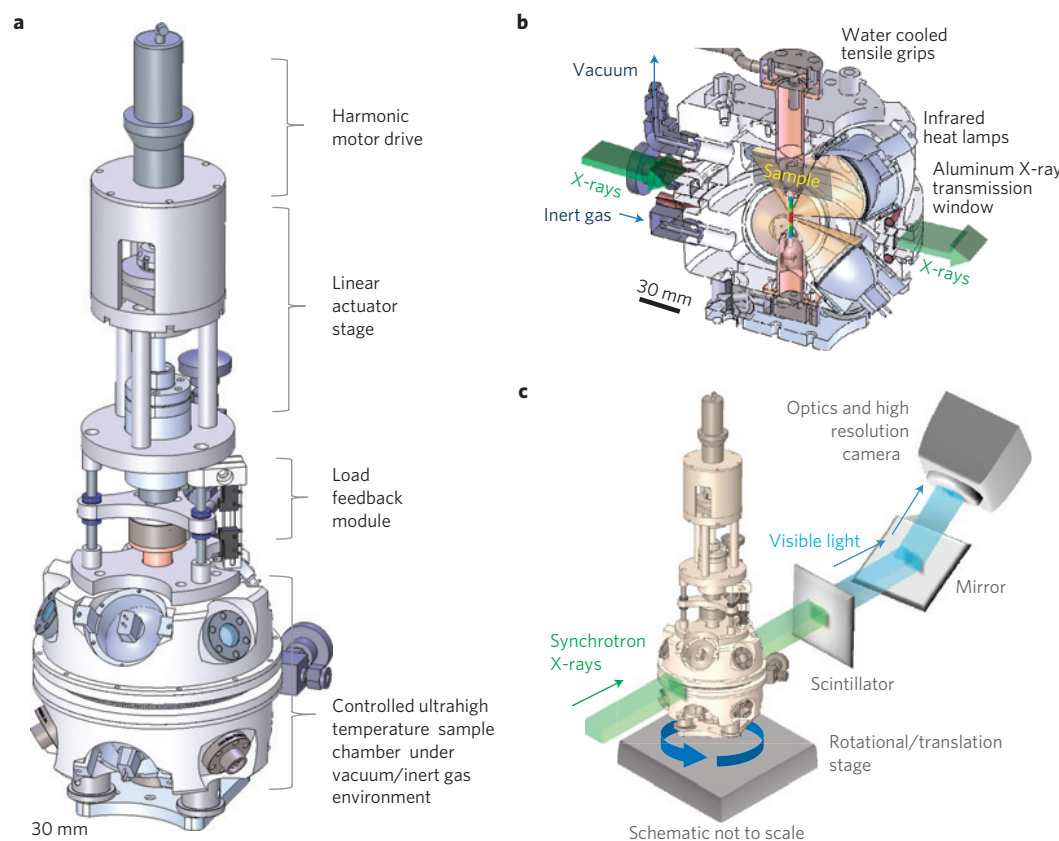


**Figure 1** | *In situ* ultrahigh temperature tensile test rig. **a**, Schematic illustration of *in situ* ultrahigh temperature tensile test rig for synchrotron X-ray computed microtomography (Beamline 8.3.2 of Advanced Light Source). **b**, Sectional view of the heating chamber illustrates X-ray transmission path through the heating chamber and sample. We have used this chamber to test materials at temperatures as high as 1,750 °C. **c**, Schematic of the rig in transmission mode for X-ray computed tomography.

represented by tests on large specimens of the phase isolated as a monolithic material.

Measurements made at high temperature are the only faithful source of the details of failure. If a test specimen is cooled to an experimentally convenient 25 °C for examination, the very act of cooling introduces thermal strains, of the order of at least 0.1–0.5% depending on composition and cooling rate, which can completely change the cracking patterns present before such cracks can be measured. *In situ* tomographic observations of deformation in an aluminium alloy have been made at temperatures as high as 555 °C (ref. 11). However, this temperature is much lower than the range of interest for ceramic composites.

In this work, we describe research to enable the mechanical and 3D structural characterization of ceramic composites *in situ*, that is, under load at ultrahigh temperatures.

#### ***In situ* X-ray $\mu$ -CT imaging at high temperature under load**

We have developed a unique facility that permits real-time  $\mu$ -CT under tensile or compressive loads at very high temperatures for the 3D imaging of materials using synchrotron X-rays. The notable features of the set-up are the ability to maintain an *in situ* temperature environment of up to 1,750 °C in inert or oxidizing atmospheres with a controlled load applied to the sample, while simultaneously imaging in real time with X-rays. The system is capable of generating 3D tomograms at a sufficiently high spatial resolution of 0.65  $\mu\text{m}$  per voxel to image structural details at the microscale and to resolve the opening displacements of internal microcracks and other forms of internal damage as a function of load.

The schematics of the *in situ* rig and its working principles are shown in Fig. 1. Detailed procedures are given in the Methods, with

further information available in the Supplementary Information. The sample is held by water-cooled grips in the centre of a vacuum-sealed cell of diameter  $\sim$ 170 mm, which can be evacuated and backfilled with a selected gas. Heating is provided by a hexapole arrangement of 150 W halogen lamps, each with an ellipsoidal reflector aimed at the centre of the cell (Fig. 1b), giving a spherical hot zone of diameter  $\sim$ 5 mm. Temperatures of test samples in the hot zone were determined from separate calibration of lamp power with thermocouples (see Supplementary Information). The waist of the cell consists of a cylindrical aluminium window (300  $\mu\text{m}$  thickness, 7 mm height), which allows X-rays to illuminate the sample and pass through to an X-ray imaging system (Fig. 1c) consisting of a scintillator coupled with microscope optics to a digital camera<sup>12</sup>. For each scan, a set of 1,200 radiographs are collected and converted to a reconstructed 3D tomographic image using inverse Radon transforms.

Images formed with the coherent synchrotron X-ray source contain a mixture of phase and absorption contrast<sup>13</sup>, which emphasizes edges and can make quantitative measurement of crack openings difficult. To minimize phase-contrast effects we used the modified Bronnikov algorithm (MBA) and filtered back-projection to obtain a 3D tomographic reconstruction of the phase signal, enabling more accurate quantitative structural measurements<sup>14</sup>.

#### **Ceramic matrix composite materials for *in situ* observations**

We chose to examine two SiC-based composites to illustrate the capability for 3D imaging under load at ultrahigh temperatures and the potential for revealing microscopic damage mechanisms that control strength and toughness. These materials were selected

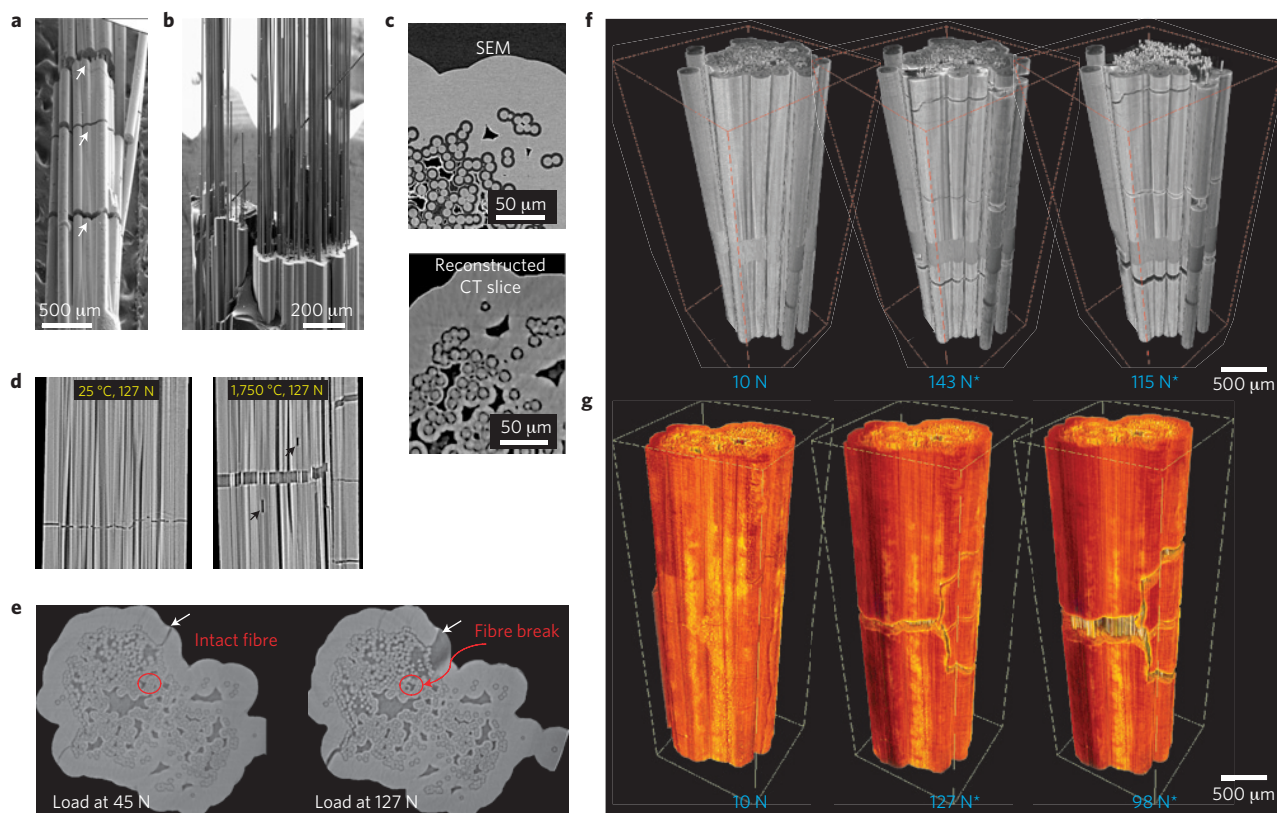


**Figure 2** | *In situ* testing of single-tow SiC-SiC composite specimens at room (25 °C) and ultrahigh (1,750 °C) temperatures. Force-displacement curves are given in Fig. 3. **a, b**, Scanning electron micrographs (SEM) of room-temperature specimen after testing. Arrows in **a** indicate multiple matrix cracks normal to the applied tensile load. The image in **b** was taken after complete separation *ex situ*. Failure is associated with pullout of fibres from the matrix. **c**, Comparison of image resolution in a reconstructed  $\mu$ -CT slice from the specimen in **a** before testing and a cross-sectional SEM image from another sample of the same composite. **d**, Longitudinal  $\mu$ -CT slices from tests at 25 and 1,750 °C (both under an applied load of 127 N), showing a single planar crack in the former and bifurcated crack with two fibre breaks (indicated by arrows) in the latter. **e**, Cross-section  $\mu$ -CT slices from the 1,750 °C specimen in **d** at two stages of loading (45 and 127 N). Red circles indicate a fibre that is intact at 45 N and broken at 127 N. **f, g**, 3D volume-rendered  $\mu$ -CT images from specimens tested at room temperature (**f**) and at 1,750 °C (**g**) at several applied tensile loads, as indicated. False colours were applied in **g** to highlight the different test temperatures. \* Load reading after first matrix crack initiated.

because of their exceptional combination of strength-to-weight ratio and high-temperature capability, which make them the most important candidate materials for future structural and engine applications at extreme temperatures.

One composite was in the form of rods ( $\sim 1$  mm diameter, 55 mm length) consisting of a single tow of SiC fibres (Nippon Carbon Hi-Nicalon Type-S, 500 fibres/tow, fibre diameter  $10\ \mu\text{m}$ ) embedded within a matrix of SiC formed by chemical-vapour infiltration (CVI). The other was in the shape of beams ( $\sim 2 \times 3 \times 55$  mm) cut from a plate of textile-based composite consisting of a woven preform of carbon fibre tows (angle interlock weave structure, T300 carbon fibres, 6,000 fibres/tow, fibre diameter  $7\ \mu\text{m}$ ) embedded in a matrix of SiC formed by a combination of CVI and infiltration/pyrolysis of a slurry of SiC particles in a polymer precursor for SiC (ref. 15). The fibres within each composite were surrounded by thin weak interphases of thickness  $\sim 0.5$ – $2\ \mu\text{m}$ ; boron nitride in  $\text{SiC}_f$ - $\text{SiC}_m$  and pyrolytic carbon in  $\text{C}_f$ - $\text{SiC}_m$ . Further details on these materials are given in the Methods.

Test specimens with 15 mm gauge length were bonded using high-temperature material similar to the matrix of the  $\text{C}_f$ - $\text{SiC}_m$  composite into threaded molybdenum grips (molybdenum was selected because its thermal expansion coefficient is similar to that of SiC over the temperature range 25–1,750 °C.), which were then mounted in a self-aligning ball-and-socket loading fixture in the test chamber. Tomography data for each specimen were collected while tensile forces were applied in steps by a displacement-controlled

loading system, increasing monotonically from 10 N until the peak load carrying capacity was exceeded. Each image consists of several tiled scans to increase the field of view. After each load step, an initial small load relaxation ( $<5\%$ ) was observed, followed by a period of constant load for the duration of the image acquisition ( $\sim 20$  min for each scan plus additional time for mechanical stabilization after moving the stage, giving a total period up to 90 min for three tiled scans). The absence of load relaxation during image acquisition at high temperature indicated that deformation due to time-dependent mechanisms such as creep were negligible in these experiments.

### Observation of damage in composite rods

The single-tow specimens were imaged with a magnification corresponding to  $0.65\ \mu\text{m}$  per voxel over a 5 mm length of test section, in tests carried out at both ambient temperature and 1,750 °C. The individual fibres and BN coatings are readily resolved in cross-sectional slices normal to the fibre tows (Fig. 2a) with no discernible difference in resolution between low- and high-temperature images. At both temperatures cracks developed in the matrix during loading, and from the 3D images they can be seen to extend continuously in the matrix through the cross-section of the composite, whereas the entire load was carried by intact fibres bridging these cracks. In these and other tests, the paths of the matrix cracks showed some variability. Most were close to a single planar surface normal to the applied load. However, some

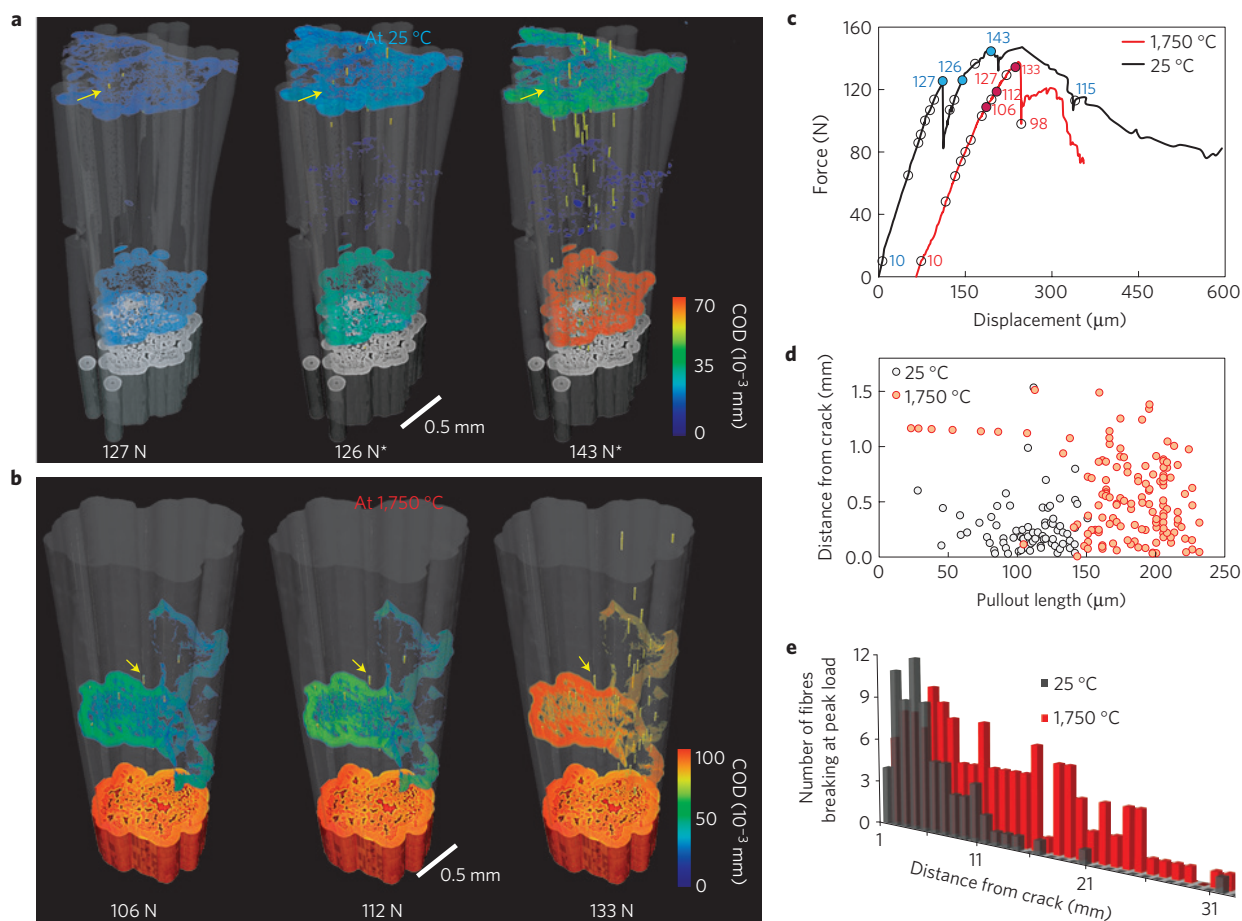


**Figure 3 | Quantification of cracks in matrix and fibres of single-tow SiC-SiC composite specimens from Fig. 2. a,b,** 3D rendering from  $\mu$ -CT data shows matrix cracks and individual fibre breaks in specimens tested at 25 °C (**a**) and 1,750 °C (**b**). The red-blue colour scheme indicates opening displacements of matrix cracks, quantified by the processing of 3D tomography data. Yellow arrows indicate cylindrical holes remaining after relaxation of broken fibres. The fibre and matrix materials have been set transparent to reveal the cracks. \* Load reading after first matrix crack initiated. **c,** Force-displacement curves from *in situ* tests in **a,b**. Red curve offset by 70  $\mu$ m for visual clarity. Hollow circles indicate acquired  $\mu$ -CT data at that load; blue and red solid circles indicate loads corresponding to images in **a,b**, respectively. **d,** Comparison of statistical data on fibre fracture at the peak loads in the specimens in **a,b**: each symbol indicates the distance of a fibre fracture from the nearest matrix crack and the separation of the fractured fibre ends after relaxation by sliding; red circles correspond to the 1,750 °C test, black circles to the 25 °C test. **e,** Histograms of the number of broken fibres as a function of distance from the closest matrix cracks at peak load. Further detailed animations of the complete sets of  $\mu$ -CT data from these two tests are included in the Supplementary Movies S1 and S2.

followed a helical path around the fibre axis, with ends joined by a crack segment parallel to the axis (top crack in Fig. 3), similar to earlier  $\mu$ -CT observations in room-temperature tests on similar composite specimens<sup>16</sup>, whereas others were branched, as in the high-temperature specimen in Fig. 2. Beginning at  $\sim$ 100 N tensile load (below peak load), broken fibres were detected at locations distributed throughout the volume of the composite. The number of broken fibres increased with increasing load, with up to 20% of the fibres breaking before peak load. Eventually, the fibres pulled out completely from the matrix (Fig. 2). The 3D images reveal a wealth of information on the events occurring in the interior of the composite during this failure process: the loads and locations at which individual fibres broke, the distances the fibres relaxed after breaking, the opening displacements of the matrix cracks, and the 3D surfaces of the matrix cracks. This can be seen in Fig. 3; further details are given in the Supplementary Movies S1 and S2 corresponding, respectively, to the ambient and high-temperature experiments.

The occurrence of crack bridging, which is essential to the toughening of these materials, is enabled by the weak BN interphase, which allows debonding and sliding between the fibres and matrix.

The magnitude of the sliding resistance dictates how multiple cracks form in the matrix<sup>17</sup>, which in turn dictates the macroscopic stress-strain response of the composite. Specifically, the friction stress determines a limiting lower-bound for the applied tensile stress at which matrix cracking can occur<sup>18–20</sup> (which relates to the onset of inelastic deformation), as well as a characteristic length over which sliding occurs and stress is transferred between the fibres and the matrix. The sliding distance determines the spacing and the opening displacements of matrix cracks as well as the relaxation of fibres that are broken within the matrix. The crack spacing and opening displacements are responsible for the nonlinear stress-strain response after the onset of inelastic behaviour.

### Quantitative analysis of $\mu$ -CT data

Although the tomography images confirm similarity in the toughening mechanism at 25 °C and at 1,750 °C, they also reveal differences that indicate a change in the sliding resistance at high temperature.

At a given load, the matrix crack-opening displacement was larger at 1,750 °C than at 25 °C (Fig. 2). As long as the sliding zones associated with adjacent cracks do not overlap and a significant

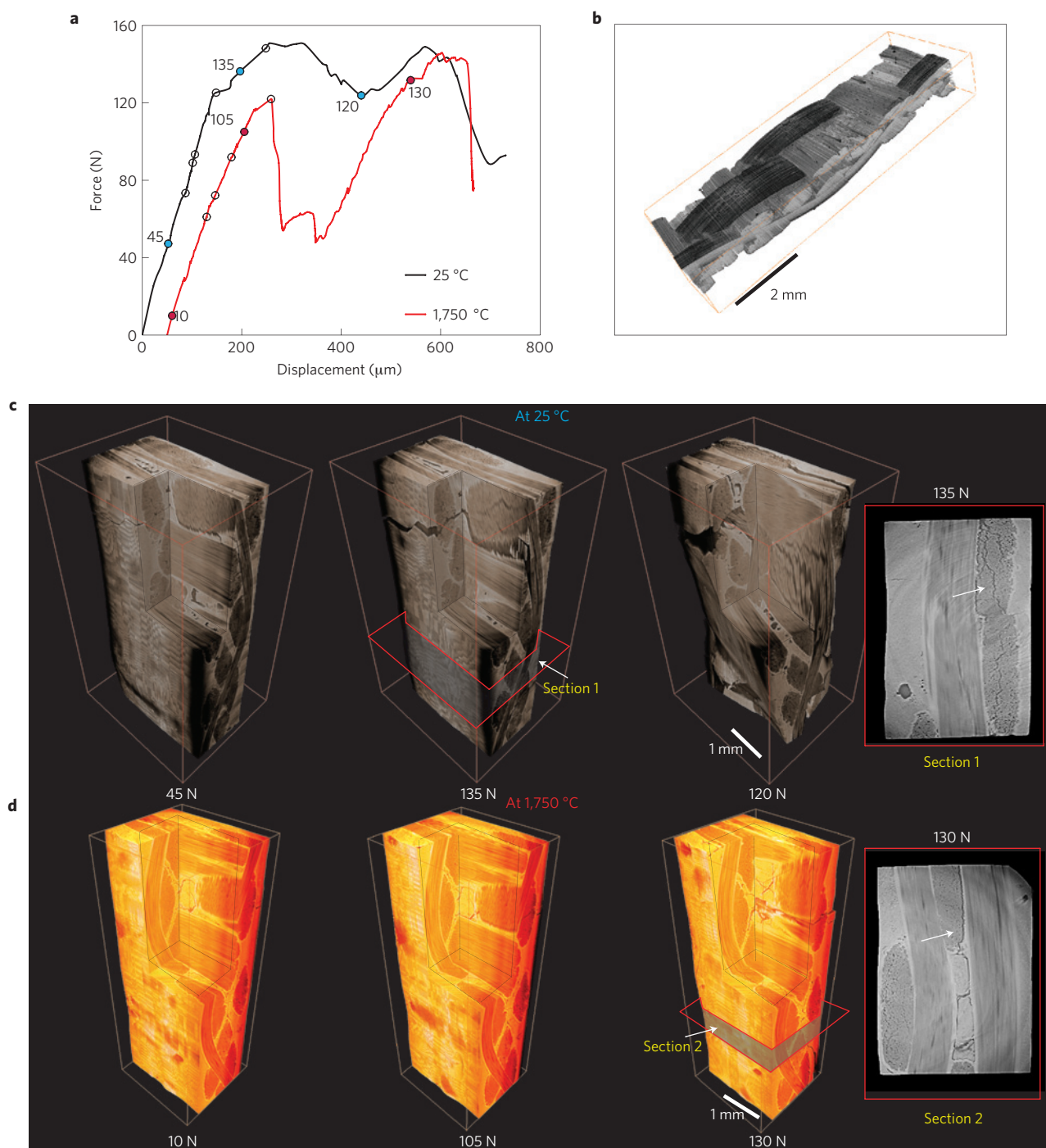


**Figure 4** | *In situ* tomography of C-SiC composite with textile-based carbon fibre reinforcements under a tensile load at 25 and 1,750 °C.

**a**, Force-displacement curves showing loads at which  $\mu$ -CT data were collected. Red curve offset by 60  $\mu\text{m}$  for visual clarity. Hollow circles indicate acquired  $\mu$ -CT data at that load; blue and red solid circles indicate loads corresponding to images in **c,d** respectively. **b**,  $\mu$ -CT image from the composite plate after partial infiltration of the SiC matrix illustrates the architecture of the woven fibre tows within the test samples. **c,d**,  $\mu$ -CT images showing development of damage in specimens tested at room temperature (**c**) and at 1,750 °C (**d**). The higher magnification slices at the right, from sections 1 and 2, show different cracking mechanisms (indicated by arrows) in the later stages of failure: at room temperature, splitting cracks grow within the axial fibre tows; at high temperature, cracks grow along the boundary between the axial fibre tows and the matrix. Further detailed animations of the complete sets of  $\mu$ -CT data from these two tests are included in the Supplementary Movies S3 and S4.

number of fibres are not broken, the magnitude of the frictional stress can be calculated from the crack-opening displacements<sup>19</sup>. From the images obtained at 127 N load (Fig. 2), we obtain frictional stresses of 2 MPa for the room-temperature test (crack opening 16  $\mu\text{m}$ ) and 0.4 MPa for the high-temperature test (crack opening 75  $\mu\text{m}$ ). Details of this calculation are given in the Supplementary

Information. From these values of frictional stress we calculate sliding lengths (and thus crack spacings) of  $\sim 3$  mm at 25 °C and  $\sim 13$  mm at 1,750 °C.

At 25 °C, multiple matrix cracks (three) formed within the test section at loads between the imaging steps at 113 and 127 N, whereas at 1,750 °C a single crack formed at 45 N load (Fig. 2). In both

cases, the crack-opening displacements continued to increase with further loading, while no new cracks were formed (confirmed also by scanning electron microscope (SEM) observations after loading to failure). The room-temperature results are consistent with observations from separate *ex situ* tests using samples with longer test sections (60 mm), which showed a distribution of cracks separated by distances between 1 and 4 mm (average 2 mm), which is consistent with calculated sliding lengths (above). In the high-temperature specimen, the observation of a single crack is also consistent with the calculated sliding length, which in this case exceeds half the gauge length.

Differences were seen in the statistical distributions of fibre failure sites and relaxation lengths at 25 and 1,750 °C (seen in Fig. 3 and Supplementary Movies S1 and S2). At high temperature, failure sites were distributed over larger distances from the matrix cracks and the relaxation distances were larger than at 25 °C. These observations are also consistent with the sliding resistance being smaller at 1,750 °C than at 25 °C. The distributed loads and positions of fibre fractures relate directly to the statistical distribution of fibre strengths<sup>21,22</sup> (if the fibre strengths were single-valued, all failures would occur at the plane of the matrix crack) and can be used to evaluate the parameters characterizing this distribution. There is currently no other way to access this information, which is critical for detecting and quantifying changes in fibre properties due to high-temperature heat treatments and possible chemical reactions during processing of the composite.

These results from *in situ* tomography provide new insight into how the 3D behaviour in SiC<sub>f</sub>-SiC<sub>m</sub> composites under tensile load differs at 25 °C and at 1,750 °C. The observed reduction in fibre sliding resistance at high temperature could potentially be caused by changes in residual stresses due to thermal expansion mismatch. However, residual stresses in this composite are expected to be small. Another possible mechanism is a change in the shear properties of the boron nitride layer between the fibres and matrix at high temperature.

### Damage evolution in textile composites

Results obtained from similar loading experiments using C<sub>f</sub>-SiC<sub>m</sub> textile composite specimens, with a larger length scale and more complex architecture than the single-tow samples, are shown in Fig. 4a–c (detailed views of cracks initiating and propagating in the room- and high-temperature specimens are shown, respectively, in the Supplementary Movies S3 and S4). Once more, differences can be seen in the development of cracks at 25 and 1,750 °C. Images here were recorded at lower resolution (1.3 μm per voxel) to allow a larger field of view. The individual carbon fibres in this composite were not visible in the sections normal or parallel to the fibre tows, because of this lower resolution and the minimal density difference between the fibres and the pyrolytic-carbon coatings. Nevertheless, the fibre tows are clearly distinguished from the denser matrix, which consists of two layers: one is a thin brighter layer of CVI SiC surrounding all of the fibre tows and the other the polymer-derived SiC that fills the remaining space. Images obtained at 25 and 1,750 °C were of identical quality. During initial loading at both temperatures, cracks formed in the matrix normal to the loading direction at positions where the matrix lays over a transverse fibre tow. With increasing load, the cracks grew through the transverse tows until they met an underlying axial tow (at loads in the range ~40–70 N), where they were deflected. At 25 °C this deflection involved formation of multiple splitting cracks (Fig. 4), which progressed incrementally along the centres of the axial tows as the load was increased to the peak value of 150 N. At 1,750 °C, the deflection of the crack at each tow involved a single crack that grew along the edge of the axial fibre tows as the load increased to 120 N, whereupon there was a large load drop. By

influencing the access of ambient gas to the internal reinforcing fibres, differences in crack paths such as these could potentially have a large effect on subsequent high-temperature oxidation damage. Further experiments are needed to determine the reason for the difference in crack paths and to assess whether similar differences in cracking behaviour are consistently observed in other loading directions.

### Outlook

In this exploratory study only a small fraction of the quantitative and statistical information potentially available in the μ-CT data sets was used. The μ-CT data contain complete quantitative information on crack paths, crack surface areas and orientations, spatial variations in the crack-opening displacements, statistics of relative spatial location of cracks and microstructural heterogeneities within the sample volume; all these parameters are critical in any analysis of fracture as they govern the toughness of the material. The challenge is to extract this information from the reconstructed 3D images in a form that can be readily used for validation of computational models and to provide calibration of material constitutive laws as input for the models. Success rests on efficient methods for processing the 3D image data with techniques such as segmentation for automated identification and representation of cracks and microstructural features. The images in Fig. 3 (and the Supplementary Movies S1 and S2) are examples of such representations obtained from the image data in Fig. 2 through the use of multiple image post-processing steps (see Supplementary Information).

We have demonstrated that *in situ* X-ray microtomography can now be used for studying the advanced materials that are being designed for future ultrahigh temperature environments. The means to acquire real-time high-resolution (up to 0.65 μm per voxel) 3D structural data for ceramic matrix composites has been presented with the ability to observe microstructure and damage under load at different hierarchical length scales (from a micrometre to several millimetres) at unprecedented temperatures (as high as 1,750 °C). The results contain vital information pertaining to the underlying failure mechanisms within ceramic composites that can be used to optimize their performance. An extension of this study would involve rigorous analysis and interpretations of the different physical phenomena occurring *in situ* under the complex environment of load and temperature. The study of time-dependent damage mechanisms involving high-temperature creep would be facilitated by reducing the scan time for image acquisition. Scan times at the Advanced Light Source (ALS) facility, where this work was performed, have recently been reduced to several minutes without loss of image quality through the use of a high-frame-rate camera and an improved high-efficiency scintillator. Even shorter scan times can be achieved at the expense of image quality by limiting the number of radiographs collected in each scan. These and other advances in synchrotron facilities show promise for enabling *in situ* tomography under near-continuous loading conditions. The capacity of validating the models developed for virtual testing through direct, real-time, non-invasive experimental observations will greatly advance our understanding and help promote innovation on these technologically important materials.

### Methods

**Materials.** The single-tow SiC<sub>f</sub>-SiC<sub>m</sub> composite specimens were fabricated at Hypertherm (Huntington Beach) by winding a SiC fibre tow on a carbon frame and by processing through CVI in two steps: the first to deposit a thin layer of boron nitride, which was doped with silicon to improve its oxidation resistance, and the second to deposit the matrix of SiC. The textile-based C<sub>f</sub>-SiC<sub>m</sub> composite was fabricated by first infiltrating a woven fabric of carbon fibre tows with a thin fibre coating of pyrolytic carbon followed by a thin layer of SiC by CVI (at Hypertherm), then forming the remaining matrix by multiple cycles of infiltration and pyrolysis of a slurry consisting of submicrometre particles of silicon carbide in

a polymer (Allylhydridopolycarbosilane) that decomposes at high temperature to form SiC. The textile fabric was a three-layer angle-interlock structure, consisting of three layers of relatively straight weft fibre tows linked together with side-by-side warp fibre tows that follow almost sinusoidal paths through the thickness of the composite. The test samples were cut from a large plate with the warp fibre tows along the axial lengths of the beams.

**$\mu$ -CT characterization.** We used the hard X-ray beamline BL 8.3.2 at the Advanced Light Source (Lawrence Berkeley National Laboratory) for the  $\mu$ -CT tomography experiments. The ultrahigh-temperature tensile rig was mounted on an air-bearing rotation stage which positioned the beam by means of translation stages. In the case of the high-temperature experiments, a non-oxidizing environment is maintained by admitting a low flow of high-purity nitrogen while pumping to  $10^{-3}$  torr. Load is applied to the sample by a stepper motor, while force and displacement are measured using an in-line load cell and a linear variable differential transformer (LVDT) sensor. A 300  $\mu\text{m}$ -thick aluminium window allows tensile forces up to 2 kN to be applied to the test sample while obtaining an X-ray transmission of  $\sim 90\%$  with the filtered white light (2.5 mm aluminium filter) used for sample illumination at a sample-to-detector distance of 150 mm. Tomography data for each specimen were collected while tensile forces were applied in steps, increasing monotonically from 10 N until the peak load carrying capacity was exceeded. Each image consists of several tiled scans to increase the field of view.

For the smaller, single tow specimens, a magnification corresponding to 0.65  $\mu\text{m}$  per voxel was used, giving a vertical field of view of approximately 1.4 mm. The full 3D dataset for this sample consists of four adjacent scans 'tiled' along the vertical direction, covering over 5.5 mm of the sample; for the textile composite specimen the data were collected in two vertical tiles with a magnification corresponding to 1.3  $\mu\text{m}$  per voxel, covering nearly 5 mm total of the specimen. Each scan consisted of multiple exposures, each of 100 ms, collected at 0.125° angular steps over a 180° rotation of the sample.

Tomographic slices were generated using a commercial reconstruction algorithm (Octopus v8; IIC UGent, Zwijnaarde). Data were processed using image processing tools in ImageJ (Rasband, W.S., ImageJ, US National Institutes of Health, Bethesda, <http://imagej.nih.gov/ij/>, 1997–2011.) and visualized in Avizo 6.1 (VSG, Visualization Sciences Group). For crack segmentation, the wavelet-FFT algorithm (referred to as xStripes)<sup>23</sup> was adapted for use in ImageJ. Transverse  $\mu$ -CT slices parallel to the axis of the fibres produced striped patterns of the fibres which are eliminated by the wavelet-FFT filter. Filtered slices contained greyscale information of cracks alone, which were binarized and further segmented to obtain the crack-opening measurements.

The magnitudes of the frictional sliding stresses were calculated from the crack-opening displacements<sup>19</sup>; details are given in the Supplementary Information.

**Temperature measurement.** Measurement of high temperatures in this test set-up is challenging as the small size of the test samples precludes directly attaching or embedding thermocouples. In these experiments, the sample temperatures in the hot zone were estimated from separate calibration tests, in which a C-type tungsten-rhenium thermocouple (maximum measurable temperature of 2,300 °C) was mounted in the top grips and translated across the field of view using the motorized loading stage, with X-ray transmission images being used to determine the thermocouple position. The variation within the central 5 mm of the field of view is approximately 150 °C at the set temperature of 1,750 °C. The operating temperature range of the furnace can be adjusted for a particular sample using calibrated voltage and current settings.

Further information on temperature measurements can be found in the Supplementary Information.

Received 24 August 2012; accepted 22 October 2012;  
published online 9 December 2012

## References

- Stock, S. R. Recent advances in X-ray microtomography applied to materials. *Int. Mater. Rev.* **53**, 129–181 (2008).
- Sakdinawat, A. & Attwood, D. Nanoscale X-ray imaging. *Nature Photon.* **4**, 840–848 (2010).
- Marshall, D. B. & Cox, B. N. Integral textile ceramic structures. *Annu. Rev. Mater. Res.* **38**, 425–443 (2008).
- Schmidt, S. *et al.* Ceramic matrix composites: A challenge in space-propulsion technology applications. *Int. J. Appl. Ceram. Technol.* **2**, 85–96 (2005).
- Mouritz, A. P., Bannister, M. K., Falzon, P. J. & Leong, K. H. Review of applications for advanced three-dimensional fibre textile composites. *Composite A* **30**, 1445–1461 (1999).
- Morscher, G. N. & Pujar, V. V. Design guidelines for in-plane mechanical properties of SiC fiber-reinforced melt-infiltrated SiC composites. *Int. J. Appl. Ceram. Technol.* **6**, 151–163 (2009).
- Zhao, J. C. & Westbrook, J. H. Ultrahigh-temperature materials for jet engines. *Mater. Res. Soc. Bull.* **28**, 622–630 (2003).
- Raj, R., Scarmi, A. & Soraru, G. D. The role of carbon in unexpected visco(an)elastic behavior of amorphous silicon oxycarbide above 1273 K. *J. Non-Cryst. Solids* **351**, 2238–2243 (2005).
- Zhuang, W., Barter, S. & Molent, L. Flight-by-flight fatigue crack growth life assessment. *Int. J. Fatigue* **29**, 1647–1657 (2007).
- Novak, M. D. & Zok, F. W. High-temperature materials testing with full-field strain measurement: Experimental design and practice. *Rev. Sci. Instrum.* **82**, 115101 (2011).
- Terzi, S. *et al.* In situ X-ray tomography observation of inhomogeneous deformation in semi-solid aluminium alloys. *Scr. Mater.* **61**, 449–452 (2009).
- Kinney, J. H. & Nichols, M. C. X-ray tomographic microscopy (XTM) using synchrotron radiation. *Annu. Rev. Mater. Sci.* **22**, 121–152 (1992).
- Langer, M., Cloetens, P., Guigay, J.-P. & Peyrin, F. Quantitative comparison of direct phase retrieval algorithms in in-line phase tomography. *Med. Phys.* **35**, 4556–4566 (2008).
- Groso, A., Abela, R. & Stampanoni, M. Implementation of a fast method for high resolution phase contrast tomography. *Opt. Express* **14**, 8103–8110 (2006).
- Berbon, Z., Rugg, K. L., Dadkhah, M. S. & Marshall, D. B. Effect of weave architecture on tensile properties and local strain heterogeneity in thin-sheet C-SiC composites. *J. Am. Ceram. Soc.* **85**, 2039–2048 (2002).
- Chateau, C. *et al.* In situ X-ray microtomography characterization of damage in SiC<sub>f</sub>/SiC minicomposites. *Compos. Sci. Technol.* **71**, 916–924 (2011).
- Budiansky, B., Evans, A. G. & Hutchinson, J. W. Fiber–matrix debonding effects on cracking in aligned fiber ceramic composites. *Int. J. Solids Struct.* **32**, 315–328 (1995).
- Morscher, G. N. Tensile stress rupture of SiC<sub>f</sub>/SiC<sub>m</sub> minicomposites with carbon and boron nitride interphases at elevated temperatures in air. *J. Am. Ceram. Soc.* **80**, 2029–2042 (1997).
- Marshall, D. B., Cox, B. N. & Evans, A. G. The mechanics of matrix cracking in brittle–matrix fiber composites. *Acta Metall. Mater.* **33**, 2013–2021 (1985).
- Morscher, G. N., Martinez-Fernandez, J. & Purdy, M. J. Determination of interfacial properties using a single-fiber microcomposite test. *J. Am. Ceram. Soc.* **79**, 1083–1091 (1996).
- Okabe, T., Nishikawa, M. & Curtin, W. A. Estimation of statistical strength distribution of carborundum polycrystalline SiC fiber using the single fiber composite with consideration of the matrix hardening. *Compos. Sci. Technol.* **68**, 3067–3072 (2008).
- Cox, B. N., Marshall, D. B. & Thouless, M. D. Influence of statistical fiber strength distribution on matrix cracking in fiber composites. *Acta Metall. Mater.* **37**, 1933–1943 (1989).
- Muench, B., Trtik, P., Marone, F. & Stampanoni, M. Stripe and ring artifact removal with combined wavelet–fourier filtering. *Opt. Express* **17**, 8567–8591 (2009).

## Acknowledgements

Work supported by the Air Force Office of Scientific Research (A. Sayir) and NASA (A. Calomino) under the National Hypersonics Science Center for Materials and Structures (AFOSR Contract No. FA9550-09-1-0477). We acknowledge the use of the X-ray synchrotron micro-tomography beam line (8.3.2) at the Advanced Light Source (ALS) at the Lawrence Berkeley National Laboratory, which is supported by the Office of Science of the US Department of Energy under contract no. DE-AC02-05CH11231.

## Author contributions

B.N.C., D.B.M. and R.O.R. conceived the project, J.R.N. and A.A.M. designed the equipment and A.H. and H.A.B. built it. D.B.M. prepared the composite samples, H.A.B. performed the experiments and analysis with assistance from A.H., A.A.M., D.L.P. and D.B.M., and H.A.B., B.N.C., D.B.M. and R.O.R. wrote the manuscript with contributions from A.A.M.

## Additional information

Supplementary information is available in the online version of the paper. Reprints and permissions information is available online at [www.nature.com/reprints](http://www.nature.com/reprints). Correspondence and requests for materials should be addressed to R.O.R.

## Competing financial interests

The authors declare no competing financial interests.